

Numerical Investigation of Radial Flow in Solar Chimney Power Plant Collector

M. K. Hasan* and A. Gross[†]

Mechanical and Aerospace Engineering Department, New Mexico State University, Las Cruces, NM 88003

The hydrodynamic stability of the radial Rayleigh-Bénard-Poiseuille flow inside the collector of solar chimney power plants has not attracted much attention in the literature. Because the ground is heated, buoyancy driven instability is possible. In addition, viscosity driven instability may occur. Temporal and spatial simulations are employed for investigating the hydrodynamic stability of the radial flow. Towards this end a new compact finite difference Navier-Stokes code is being developed. Square channel flow simulations were performed for code validation purposes using both the new code and an existing finite-volume code. For certain Reynolds and Rayleigh number combinations transverse rolls or longitudinal rolls appear while for others the flow remains stable. A Fourier mode decomposition of the wall-normal velocity component at mid-channel height reveals linear (exponential) growth for the unstable modes and nonlinear interactions once the mode amplitudes exceed a certain threshold. The present square channel flow results are consistent with the neutral curves from the linear stability theory analysis by Gage and Reid. Simulations were also carried out for the collector of a 1:30 scale model of the Manzanares solar chimney power plant at the University of Arizona. The Rayleigh number is well above the critical Rayleigh number and steady longitudinal rolls appear shortly downstream of the collector inflow.

I. Introduction

The increasing demand of energy is one of the main challenges facing humanity. The limited amount of conventional non-renewable energy resources and the associated environmental pollution provide motivation for the development of sustainable technologies that utilize clean energy resources. The solar chimney power plant (SCPP) is a promising technology that represents a complete sustainable energy pathway from solar irradiation to electrical power. The SCPP is based on simple principles and can be built from readily available construction materials by unskilled workers which makes it an especially attractive technology for developing countries. The bottom surface of a radial collector absorbs the incoming solar irradiation and heats the air under the collector cover. The density difference between the hot air at the collector outlet and the cooler air in the vicinity of the plant creates a buoyancy force that drives the hot air through a central chimney. Turbines installed at the chimney entrance introduce a pressure drop and generate mechanical power which is converted into electrical power via generators.

The most alluring feature of SCPPs is that the generated power is proportional to the product of collector area and chimney height which distinguishes SCPPs from photovoltaic (PV) and concentrated solar power (CSP) systems for which the power scales with the collector area only. Moreover, the ground under the collector of SCPPs can be utilized for greenhouse cultivation and the collector cover can serve as a rain water harvesting device. Finally, the collector is also reducing wind erosion. A demonstration plant was designed and constructed by Schlaich, Bergermann and Partner in Manzanares, Spain, in the 1980s with funding from the German Science Foundation and the Spanish government. The plant was operated between 1982 and 1989 and generated approximately 50kW of electrical power.¹⁻⁴ According to Schlaich, the generated power can be estimated as

$$P = \eta_c \eta_t \frac{2}{3} g \frac{H_t \pi R_c^2 I}{c_p T_\infty} \,, \tag{1}$$

^{*}Graduate Research Assistant. Member AIAA.

[†]Assistant Professor. Senior Member AIAA.

where η_c and η_t are the collector and turbine efficiency, g is the gravitational acceleration, I is the solar irradiation, and T_{∞} is the ambient temperature. The power, P, scales with the collector area, πR_c^2 and chimney height, H_t . The geometric dimensions of the Manzanares plant (1:1 scale) are provided in Tab. 1.

To investigate the flow physics of the radial SCPP collector flow a scientifically instrumented 1:30 scale model of the Manzanares plant was designed and built by H. Fasel and co-workers at the Aerospace and Mechanical Engineering Department at the University of Arizona.⁵ The dimensions of the scaled plant ("model") are also included in Tab. 1.

	Collector radius	Collector height	Chimney height	Chimney diameter
Manzanares (1:1 scale)	122m	2m	198m	10m
Model (1:30 scale)	$4.07\mathrm{m}$	$0.067 \mathrm{m}$	$6.6 \mathrm{m}$	$0.33 \mathrm{m}$

Table 1. Geometric dimensions of full-size and model SCPP.

Numerical investigations of the time-dependent and transient (diurnal cycle) nature of the flow inside the SCPP have been carried out by numerous researchers. Reynolds-averaged Navier-Stokes (RANS) calculations have been performed by Pastohr et al.⁶ Ming et al.⁷ established an analytical model for the collector to investigate the effect of various parameters on the differential (between chimney inlet and ambient) pressure as well as the power and plant efficiency and compared the results with data obtained from RANS calculations. Later Ming et al.⁸ carried out RANS calculations with a standard k- ϵ turbulence model to analyze a SCPP with energy storage layers. Ming et al.⁸ also performed RANS calculations for investigating the effect of crosswind on the SCPP system performance.⁹ The effect of solar irradiation and turbine pressure drop on the power output for the Manzanares SCPP was investigated by Xu et al.¹⁰ To the authors best knowledge none of the previous research has addressed hydrodynamic instabilities of the collector flow that may lead to large-scale coherent structures which may have a profound effect on the collector efficiency.

Channel flows with wall-normal temperature gradient and gravitational field are known as Rayleigh-Bénard-Poiseuille (RBP) flows. The radial flow under the collector may thus be referred to as a radial RBP flow. Because the ground is heated and the buoyancy force opposes the gravitational acceleration the flow can exhibit buoyancy driven instability. The relevant dimensionless numbers are the Reynolds number,

$$Re = \frac{u_b 2h}{\nu} \,, \tag{2}$$

with bulk velocity, u_b , channel height, h, and kinematic viscosity, ν , the Rayleigh number,

$$Ra = \frac{gh^3\gamma\Delta T}{\nu\alpha}\,, (3)$$

with gravitational acceleration, g, volumetric thermal expansion coefficient, γ , temperature difference, ΔT , and thermal diffusivity, α , and the Prandtl number,

$$Pr = \frac{\nu}{\alpha}.\tag{4}$$

Gage and Reid¹¹ carried out a comprehensive linear stability theory (LST) analysis of the plane RBP flow in a two-dimensional (2-D) channel. Neutral curves were obtained for two different instability modes. For $Re > Re_c = 5,400$ and $Ra < Ra_c = 1,708$, a viscous instability was discovered leading to the amplification of Tollmien-Schlichting (T-S) waves. For this regime, 2-D waves were found to grow faster than three-dimensional (3-D) oblique waves. The resulting flow structures, after the disturbance amplitudes have saturated, are referred to as transverse rolls.

For $Re < Re_c$ and $Ra > Ra_c$, three-dimensional longitudinal waves were found to be amplified and the resulting flow structures are referred to as longitudinal rolls. For this regime, the 3-D disturbances were found to grow faster than the 2-D disturbances. The Gage and Reid findings were validated by numerous experiments¹² and simulations.¹³ The nonlinear interaction of longitudinal and transverse rolls was analyzed by Fujimura and Kelly.¹⁴ Longitudinal rolls must be expected below the critical Reynolds number for the viscous instability as long as the Rayleigh number, aspect ratio, and background noise level are high enough and nonlinear effects are not significant.

The lateral confinement (spanwise extent) of channels of engineering interest is always limited. For channels with a width-to-height ratio of less than five, transverse convection rolls were observed for Reynolds

numbers below the critical Reynolds number for the T-S instability (e.g., Luijkx et al. ¹⁵). A stability analysis by Nicolas et al. ¹⁶ showed that "lateral confinement" stabilized the flow with respect to longitudinal rolls (increasing the critical Rayleigh number for longitudinal rolls beyond 1,708). A transition from "convective" to "absolute" instability was discovered for the transverse rolls by Lücke and Kamps. ¹⁷ Carriére and Monkewitz ¹⁸ showed that longitudinal rolls never become "absolutely" unstable. The mode reaching zero-group velocity always corresponds to transverse rolls.

The understanding of the flow physics and especially the inherent primary instabilities of the radial RBP flow in the collector is of great importance as it provides the critical parameters that determine if and when flow structures form. While the plane RBP flow has been investigated in great detail, research on inward radial channel flow with convection is sparse. Van Santen et al. 19,20 considered the strongly decelerated outward radial flow between two horizontal plates. Direct numerical simulations (DNS) and experiments were employed for investigating the formation of transverse (axisymmetric) and longitudinal rolls resulting from the onset of buoyancy-driven instability. 19,20 An interesting outcome was that transverse rolls are favored in radial channel flow at very low Reynolds numbers when the Rayleigh number is above critical. This is quite surprising since it is in contradiction to the plane channel flow results by Gage and Reid. 11

Although some of the extensive research for plane RBP flows may carry over to radial channel flows with convection, differences must be expected, since for the inward radial flow, the circumference and hence the channel aspect ratio decreases in the streamwise direction. As a result the flow is strongly accelerated (which usually has a stabilizing effect) and the velocity profile changes in the streamwise direction which introduces non-parallel effects. Fasel et al.²¹ carried out RANS calculations for various scales to validate the scaling laws.¹ Meng et al.²² performed an implicit large eddy simulation (ILES) for a 1:33 scale model of the Manzanares SCPP. The mean flow was found to be consistent with the mean flow of an earlier RANS calculation by Fasel et al. for the same scale.²¹ The ILES revealed longitudinal rolls that arise likely as a result of a buoyancy-driven instability.

The present paper constitutes a continuation of the earlier research by Fasel and co-workers.^{5,21,22} A new highly accurate compact finite difference computational fluid dynamics (CFD) code was developed for investigating the temporal stability of RBP flows. The new code as well as an existing finite volume code were employed for square channel flow simulations and the stability behavior of both 2-D and 3-D waves was compared with the neutral curves by Gage and Reid.¹¹ Secondly, collector flow simulations are proposed as a low-cost alternative to entire 3-D simulations of the 1:30 scale SCPP at the University of Arizona.⁵

II. Methodology

A. Governing Equations

The compressible Navier-Stokes equations in conservative form can be written in vector form,

$$\frac{\partial \mathbf{Q}}{\partial t} + \frac{\partial \mathbf{E}}{\partial x} + \frac{\partial \mathbf{F}}{\partial y} + \frac{\partial \mathbf{G}}{\partial z} = \mathbf{H}, \qquad (5)$$

with state vector,

$$\mathbf{Q} = \begin{bmatrix} \rho \\ \rho u \\ \rho v \\ \rho w \\ \rho e \end{bmatrix}, \tag{6}$$

and flux vectors,

$$\mathbf{E} = \begin{bmatrix} \rho u \\ \rho u^2 + p - \tau_{xx} \\ \rho uv - \tau_{xy} \\ \rho uw - \tau_{xz} \\ y(\rho e + p) - u\tau_{xx} - v\tau_{xy} - w\tau_{xz} + q_x \end{bmatrix}, \tag{7}$$

$$\mathbf{F} = \begin{bmatrix} \rho v \\ \rho v u - \tau_{xy} \\ \rho v^2 + p - \tau_{yy} \\ \rho v w - \tau_{yz} \\ v(\rho e + p) - u \tau_{xy} - v \tau_{yy} - w \tau_{yz} + q_y \end{bmatrix},$$
(8)

and

$$\mathbf{G} = \begin{bmatrix} \rho w \\ \rho w u - \tau_{xz} \\ \rho w v - \tau_{yz} \\ \rho w^2 + p - \tau_{zz} \\ w(\rho e + p) - u \tau_{xz} - v \tau_{yz} - w \tau_{zz} + q_z \end{bmatrix} . \tag{9}$$

Here, u, v, and w are the velocities in the x, y, and z direction, ρ is the density, p is the static pressure, and T is the temperature. The total energy is $e = \epsilon + 1/2(u^2 + v^2 + w^2)$, where $\epsilon = c_v T$ is the internal energy. The source term vector,

$$\mathbf{H} = \begin{bmatrix} 0 \\ \frac{\partial p}{\partial x} \\ g(\rho_{ref} - \rho) \\ 0 \\ u\frac{\partial p}{\partial x} + vg(\rho_{ref} - \rho) \end{bmatrix}, \tag{10}$$

contains a $\partial p/\partial x$ term that compensates for the streamwise pressure drop resulting from the viscous losses (only for the temporal simulations), and a buoyancy term, $g(\rho_{ref} - \rho)$ (Boussinesq approximation), with gravitational acceleration, $g = 9.81 m/s^2$. The shear stress tensor components are,

$$\tau_{xx} = \mu \frac{2}{3} \left(2 \frac{\partial u}{\partial x} - \frac{\partial v}{\partial y} - \frac{\partial w}{\partial z} \right) \tag{11}$$

$$\tau_{yy} = \mu \frac{2}{3} \left(2 \frac{\partial v}{\partial y} - \frac{\partial u}{\partial x} - \frac{\partial w}{\partial z} \right) \tag{12}$$

$$\tau_{zz} = \mu \frac{2}{3} \left(2 \frac{\partial w}{\partial z} - \frac{\partial u}{\partial x} - \frac{\partial v}{\partial u} \right) \tag{13}$$

$$\tau_{xy} = \mu \left(\frac{\partial u}{\partial y} + \frac{\partial v}{\partial x} \right) \tag{14}$$

$$\tau_{xz} = \mu \left(\frac{\partial u}{\partial z} + \frac{\partial w}{\partial x} \right) \tag{15}$$

$$\tau_{yz} = \mu \left(\frac{\partial v}{\partial z} + \frac{\partial w}{\partial y} \right),\tag{16}$$

with dynamic viscosity, μ , and the heat flux vector components are,

$$q_x = -k \frac{\partial T}{\partial x} \tag{17}$$

$$q_y = -k \frac{\partial T}{\partial u} \tag{18}$$

$$q_z = -k \frac{\partial T}{\partial z} \,, \tag{19}$$

with thermal conductivity, k. The set of equations is closed by the ideal gas equation,

$$p = \rho RT, \tag{20}$$

with gas constant, R.

Discretization

Two in-house developed computational fluid dynamics (CFD) codes were employed for solving the governing equations: An established versatile finite-volume code and a newly developed customized highly-accurate compact finite difference code. All simulations were performed either on a local work station or on the XSEDE²³ high performance computing (HPC) system Comet.

Finite Volume Code

As a reference, simulations were carried out with a finite volume code by Gross and Fasel.²⁴ The convective terms were computed with a ninth-order-accurate upwind scheme. The viscous terms were discretized with fourth-order accuracy. A second-order accurate implicit Adams-Moulton method was employed for time integration. The resulting system of equations was solved iteratively. In this paper, this method is referred to as "old code".

Compact Finite Difference Code

A new highly accurate Navier-Stokes code was developed specifically for the simulation of temporal RBP flows. The code employs fourth-order-accurate compact finite differences in the wall-normal direction,

$$u'_{i-1} + 4u'_{i} + u'_{i+1} = \frac{3u_{i+1} - 3u_{i-1}}{\Delta \eta}$$

$$u''_{i-1} + 10u''_{i} + u''_{i+1} = \frac{12u_{i+1} - 24u_{i} + 12u_{i-1}}{\Delta \eta^{2}},$$
(21)

$$u_{i-1}'' + 10u_i'' + u_{i+1}'' = \frac{12u_{i+1} - 24u_i + 12u_{i-1}}{\Delta \eta^2},$$
(22)

where the primes indicate derivatives in computational space (coordinate, η , with $\Delta \eta = 1$). The resulting tridiagonal systems of equations are solved with the Thomas algorithm. Derivatives in the streamwise (xcoordinate) and spanwise (z-coordinate) direction are calculated in Fourier space. The forward and backward Fourier transforms are computed out with fast Fourier transform (FFT) subroutines by Sorensen et al. ^{25,26}

A coordinate transformation is employed in the wall-normal direction (grid line index, j; coordinate in computational space, $\eta = j$; $\Delta \eta = 1$) that clusters grid points near the walls. A total of J grid points are distributed in the wall-normal direction,

$$y_j = \left[\frac{\tan^{-1}(jc - f_1)}{f_2} + 1\right] \times \frac{h}{2},$$
 (23)

where h is the channel height, c is a user specified constant, $f_1 = Jc/2$, and $f_2 = \tan^{-1}(f_1)$. The first and second derivatives of the computational coordinate with respect to the physical coordinate are,

$$\frac{\partial \eta}{\partial y} = 2\frac{f_2}{ch} \left\{ 1 + \tan^2 \left[\left(\frac{2y}{h} - 1 \right) f_2 \right] \right\}$$
 (24)

$$\frac{\partial^2 \eta}{\partial y^2} = 4 \frac{f_2}{h} \frac{\partial \eta}{\partial y} \tan \left[\left(\frac{2y}{h} - 1 \right) f_2 \right]. \tag{25}$$

The derivatives in physical space can then be obtained from

$$\frac{\partial u}{\partial y} = u' \frac{\partial \eta}{\partial y} \tag{26}$$

$$\frac{\partial^2 u}{\partial y^2} = u'' \left(\frac{\partial \eta}{\partial y}\right)^2 + u' \frac{\partial^2 \eta}{\partial y^2}. \tag{27}$$

By bringing the flux derivatives to the right-hand-side, the governing equations can be written as,

$$\frac{\partial \mathbf{Q}}{\partial t} = \mathbf{R} = \left(\mathbf{H} - \frac{\partial \mathbf{E}}{\partial x} - \frac{\partial \mathbf{F}}{\partial y} - \frac{\partial \mathbf{G}}{\partial z} \right). \tag{28}$$

A fourth-order-accurate explicit low-storage Runge-Kutta method is employed for time integration, ²⁷

$$\mathbf{Q}_1 = \mathbf{Q}^n + \frac{\Delta t}{2} \mathbf{R}(\mathbf{Q}^n) \tag{29}$$

$$\mathbf{Q}_2 = \mathbf{Q}^n + \frac{\Delta t}{2} \mathbf{R}(\mathbf{Q}_1)$$

$$\mathbf{Q}_1 \quad \Leftarrow \quad \mathbf{Q}_1 + 2\mathbf{Q}_2 \tag{30}$$

$$\mathbf{Q}_2 = \mathbf{Q}^n + \Delta t \mathbf{R}(\mathbf{Q}_2)$$

$$\mathbf{Q}_1 \quad \Leftarrow \quad \frac{1}{2}(-\mathbf{Q}^n + \mathbf{Q}_1 + \mathbf{Q}_2) \tag{31}$$

$$\mathbf{Q}^{n+1} = \mathbf{Q}_1 + \frac{\Delta t}{6} \mathbf{R}(\mathbf{Q}_2). \tag{32}$$

Here, n and n+1 are the old and new time step.

The velocities at the top and bottom wall are zero. Assuming steady wall-tangential flow $(\partial \rho v/\partial t = 0)$ and $\partial/\partial x = 0$, the wall-normal momentum equation at the walls simplifies to

$$\frac{\partial p}{\partial y} = g(1 - \rho). \tag{33}$$

When the pressure differential is discretized with a one-sided third-order accurate finite difference stencil, the wall pressure becomes,

$$p_0 = \frac{6g\frac{\partial y}{\partial \eta} + 18p_1 - 9p_2 + 2p_3}{11 + \frac{6g}{RT_0}\frac{\partial y}{\partial \eta}} \ . \tag{34}$$

C. Channel Flow Relationships

The hydraulic diameter for a 2-D channel flow (height h and span b) is defined as

$$D_h = \frac{4b \times h}{2(b+h)} \,. \tag{35}$$

For a channel with infinite width or span $(b \to \infty)$, $D_h = 2h$. The bulk velocity is defined as

$$u_b = \frac{1}{h} \int u \, dy \,. \tag{36}$$

From the x-momentum equation for a laminar 2-D channel flow,

$$\nu u_{yy} = \frac{1}{\rho} \frac{\partial p}{\partial x},\tag{37}$$

the velocity profile can be found by integration.

$$u = \frac{1}{2\rho\nu} \frac{\partial p}{\partial x} \left(y^2 - hy \right) \,. \tag{38}$$

The maximum velocity is obtained at the channel half-height,

$$u_{max} = -\frac{h^2}{8\rho\nu} \frac{\partial p}{\partial x}.$$
 (39)

The velocity profile expressed in terms of the maximum velocity is

$$u = 4u_{max} \left[\frac{y}{h} - \left(\frac{y}{h} \right)^2 \right] . \tag{40}$$

From this the bulk velocity for the laminar profile can be obtained,

$$u_b = \frac{2}{3}u_{max}. (41)$$

The skin-friction coefficient for the laminar 2-D channel flow can be computed from the near-wall gradient of the velocity profile,

$$\frac{\partial u}{\partial y} = 4u_{max} \left(\frac{1}{h} - 2\frac{y}{h^2} \right) \,. \tag{42}$$

At the wall,

$$\frac{\partial u}{\partial y} = 4 \frac{u_{max}}{h} \,, \tag{43}$$

and the skin-friction coefficient based on the bulk velocity becomes,

$$c_f = \frac{\rho \nu \frac{\partial u}{\partial y}}{\frac{1}{2}\rho u_b^2} = 12 \frac{\nu}{u_b h} \,. \tag{44}$$

The Darcy friction factor f is defined as

$$\frac{\partial p}{\partial x} = -\frac{1}{2}\rho u_b^2 \frac{f}{D_h} \,. \tag{45}$$

From a control volume analysis in the streamwise direction for the 2-D channel flow,

$$hb\frac{\partial p}{\partial x}dx + \tau 2bdx = 0, \qquad (46)$$

the skin friction can be obtained,

$$\tau = -\frac{h}{2} \frac{\partial p}{\partial x} \,. \tag{47}$$

Making use of the friction factor,

$$\tau = \frac{h}{2} \frac{1}{2} \rho u_b^2 \frac{f}{D_h} = \frac{f}{8} \rho u_b^2 \,, \tag{48}$$

is obtained which is valid for both laminar and turbulent channel flow. With this the skin-friction coefficient becomes

$$c_f = \frac{\tau}{\frac{1}{2}\rho u_b^2} = \frac{f}{4} \,. \tag{49}$$

D. Non-Dimensionalization

The governing equations were made dimensionless with a reference velocity, v_{ref} , a reference length scale, L_{ref} , a reference temperature, T_{ref} , and a reference density, ρ_{ref} . Pressure was made dimensionless with $\rho_{ref}v_{ref}^2$.

1. Square Channel Flow Simulations

Several laminar square channel flow simulations were performed for code validation purposes. The Reynolds number based on bulk velocity and hydraulic diameter is

$$Re = \frac{u_b 2h}{\nu} \,. \tag{50}$$

Gage and Reid¹¹ based their Reynolds number on the maximum velocity and the channel half height,

$$Re_{GR} = \frac{u_{max} \frac{h}{2}}{\nu} \,. \tag{51}$$

Using the expression for the bulk velocity, the Reynolds number for a laminar 2-D channel flow becomes

$$Re = \frac{4}{3} \frac{u_{max}h}{u} = \frac{8}{3} Re_{GR}. {52}$$

For the present simulations the bulk velocity was taken as reference velocity, $v_{ref} = u_b$, and the channel half-height was taken as reference length, $L_{ref} = h/2$. The resulting reference Reynolds number is

$$Re_{ref} = \frac{v_{ref}L_{ref}}{\nu} = \frac{u_b \frac{h}{2}}{\nu} = \frac{1}{4}Re$$
. (53)

For laminar flow $c_f = 24/Re$ and therefore $f = 96/Re = 24/Re_{ref}$. The negative pressure gradient made dimensionless with the reference length, $L_{ref} = h/2$, and the bulk velocity is

$$-\frac{\partial p}{\partial x}\frac{\frac{h}{2}}{\rho u_b^2} = \frac{f}{8} = \frac{dp}{dx}.$$
 (54)

For the square channel flow simulations this expression is added as a source term to the right-hand-side of the streamwise momentum equation to maintain a constant bulk velocity.

The Rayleigh number is defined as

$$Ra = \frac{\gamma h^3 g \Delta T}{\nu \alpha} \,, \tag{55}$$

where $\gamma = 1/T_{av}$ with $T_{av} = (T_{hot} + T_{cold})/2$ is the thermal expansion coefficient for a perfect gas, $\Delta T = T_{hot} - T_{cold}$, is the temperature difference between the bottom and top wall, and α is the thermal diffusivity. The Prandtl number is defined as

$$Pr = \frac{\nu}{\alpha} \,. \tag{56}$$

The Rayleigh number can be written as

$$Ra = Re^{2\frac{\Delta T}{T_{av}} \left(\frac{h}{L_{ref}}\right)^{3} \left(g\frac{L_{ref}}{v_{ref}^{2}}\right)}{Pr},$$
(57)

where gL_{ref}/v_{ref}^2 is the dimensionless gravitational acceleration. The bottom and top wall temperatures were 350K and 300K, respectively. The latter was also chosen as reference (and ambient) temperature. In accordance with Gage and Reid¹¹ the Prandtl number was set to 1 and the reference Mach number was set to 0.3.

2. Simulation of Entire SCPP Model

An earlier simulation by Meng et al.²² for the 1:30 scale model of the Manzanares plant at the University of Arizona⁵ was continued. Different from the approach chosen for the square channel flow simulations, the governing equations were made dimensionless with the chimney diameter, d=0.02646m, a reference velocity of 0.3473m/s, the density at the chimney outflow, and the temperature of the upper cooler collector surface, T=300K, which was identical to the ambient temperature. The reference Reynolds number is $Re = \rho_{ref}v_{\infty}d/\mu_{ref} = 57,790$. For the chosen non-dimensionalization a Rayleigh number of $Ra = gd^3\Delta T/(\alpha\nu_{ref}T_{av}) = 1.391 \times 10^6$, and a non-dimensional gravitational acceleration of $gd/v_{ref}^2 = 0.2438$ are obtained. The reference Prandtl and Mach number were 0.72 and 0.001.

3. Collector Simulations

To cut down on the computational expense of the full SCPP simulations, simulations of the collector only were carried out as well. For the collector simulations, length scales were made dimensionless with the collector half height, $h = 6.604 \times 10^{-4} m$, velocities were made dimensionless with the collector inflow velocity, 17.37m/s, and the temperature was made dimensionless with the temperature of the collector top surface, T=300K (which matched the ambient temperature). The reference Reynolds and Rayleigh number were $Re = v_{ref}L_{ref}/\nu_{ref} = 721.1$ and $Ra = gL_{ref}^3\Delta T/(\alpha\nu_{ref}T_{av}) = 23.87 \times 10^6$ and the dimensionless gravitational acceleration was $gL_{ref}/v_{ref}^2 = 2.686$. The reference Mach number was set to 0.05 and the Prandtl number was 0.72.

E. Computational Domain

Computational grids for the simulations of the square channel flow, the entire SCPP, and the collector are shown in Figs. 1-3. For the square channel flow simulations the analytical grid function (Eq. 23) with c=0.2 was employed in the wall-normal direction and the streamwise and spanwise grid extent were varied. For the simulation of the entire SCPP the two-domain computational grid by Meng et al.²² was used. The azimuthal grid opening angle is 15deg for the collector domain and 45deg for the chimney and center cone domain. A wedge shaped grid with 15deg grid opening angle was generated for the collector simulations (no

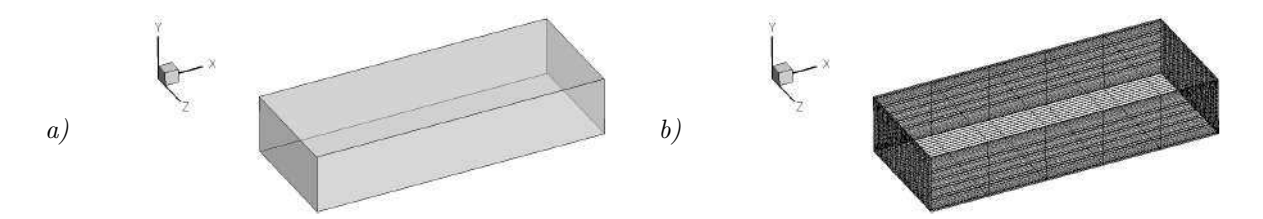


Figure 1. (a) Typical computational domain boundaries and (b) details of mesh for square channel flow simulations.

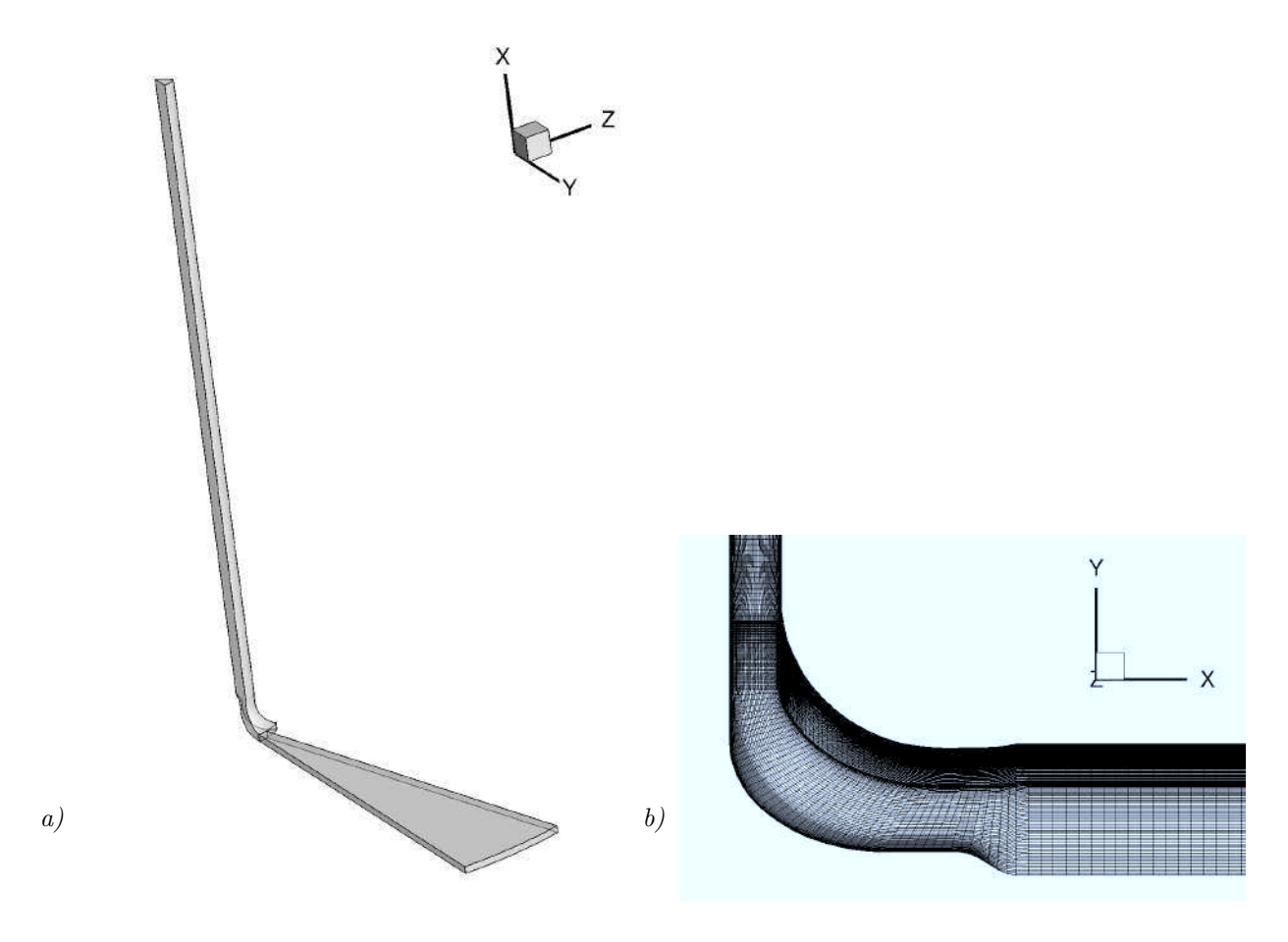


Figure 2. (a) Computational domain boundaries and (b) details of mesh for entire SCPP simulation.

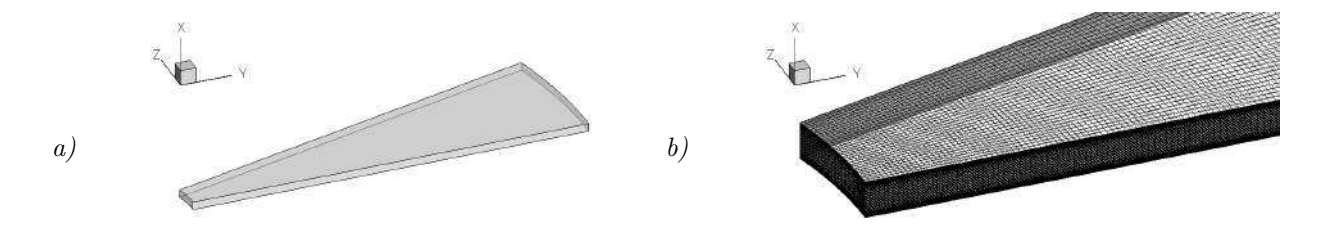


Figure 3. (a) Computational domain boundaries and (b) details of mesh for collector simulations.

chimney). Grid points were clustered near the lower and upper wall. The number of cells in the streamwise, wall-normal, and azimuthal direction and the near-wall grid resolution in wall units for the entire SCPP and the collector flow simulations are presented in Tab. 2.

Case		Number of cells	Near wall grid resolution
Entire SCPP simulation	Collector	$512 \times 64 \times 33$	$\Delta x_{max}^{+} = 76, \Delta y_{max}^{+} = 0.54, \Delta z_{max}^{+} = 26$
	Chimney	$433\times64\times99$	$\Delta x_{max}^+ = 120, \Delta y_{max}^+ = 1.6, \Delta z_{max}^+ = 10$
Collector simulation		$256\times64\times32$	$\Delta x_{max}^+ = 32, \Delta y_{max}^+ = 1.6, \Delta z_{max}^+ = 44$

Table 2. Number of cells and near-wall grid resolution in wall units.

F. Boundary Conditions

For all simulations the top (collector cover) and bottom wall (ground) temperature were set to 300K and 350K, respectively. The ambient temperature was set to 300K. No slip and no penetration boundary conditions were enforced at all walls.

1. Square channel flow simulation

Periodicity conditions were employed in the streamwise and spanwise directions.

2. Entire SCPP and Collector Simulation

At the collector inlet a parabolic velocity profile and a constant temperature of 300K were prescribed and the static pressure was extrapolated from inside the computational domain (assuming a zero pressure gradient in the streamwise direction). A characteristics-based boundary condition²⁸ was employed at the outflow boundary (chimney or collector outflow depending on simulation). Flow periodicity was enforced in the azimuthal direction.

III. Results

A. Square Channel Flow Simulations

Square channel flow simulations were performed for cross-validating the two Navier-Stokes codes (old and new code). Different Reynolds and Rayleigh number combinations close to the 2-D and 3-D neutral loops in the Gage and Reid¹¹ stability diagram were considered. The relevant parameters for the different investigated unstable and stable cases are listed in Tab. 3 and plotted with the Gage and Reid¹¹ neutral curves in Fig. 4. In Fig. 4, λ denotes the wave angle. For $Re > Re_c = 5$, 400 and $Ra < Ra_c = 1$, 708 2-D waves (λ =0deg) are most unstable; For $Ra > Ra_c = 1$, 708 and $Re < Re_c = 5$, 400 3-D waves (λ =90deg) are most unstable. Of course, in 2-D simulations the 3-D waves are artificially suppressed. For the 2-D simulations ($Re < Re_c$) disturbance growth is expected if \sqrt{Ra} is above the λ =0deg neutral curve; For the 3-D simulations, disturbance growth is expected if \sqrt{Ra} is above the λ =90deg neutral curve. The cases were chosen such the flow is either (1) stable, (2) unstable w.r.t. 3-D waves but stable w.r.t. 2-D waves, and (3) unstable w.r.t. both 2-D and 3-D waves.

The old and new code were cross-validated for a reference Reynolds number of 100 (cases 1-4). Important for the cross-validation is an accurate match of the baseflow profiles. Figure 5 confirms that the baseflow profiles are in good agreement. The slight asymmetry of the velocity profiles is caused by the temperature gradient which results in a minor variation of the viscosity in the wall-normal direction. The pressure and density profiles are consistent with $\partial p/\partial y = g(1-\rho)$.

Because the wall-normal velocity component is zero for steady channel flow, it can be used to track the growth or decay of disturbances. Therefore, the wall-normal velocity at the mid-channel height was taken as disturbance velocity, v'. In linear stability theory a wave ansatz,

$$v' = V(y)e^{i(\alpha x + \beta z - \omega t)}, \tag{58}$$

is made for the disturbances. Here, $\alpha = \alpha_r + i\alpha_i$ is the streamwise wavenumber, $\beta = \beta_r + i\beta_i$ is the spanwise wavenumber, and $\omega = \omega_r + i\omega_i$ is the frequency. For the present temporal simulations the disturbances grow in time and thus $\alpha_i = \beta_i = 0$ and ω_i is the temporal growth rate. The streamwise and spanwise wavenumber are related to the streamwise and spanwise wavelength via $\alpha_r = 2\pi/\lambda_x$ and $\beta_r = 2\pi/\lambda_z$. The frequency is related to the period via $\omega_r = 2\pi/T$. For the present simulations, the mode amplitude was either directly

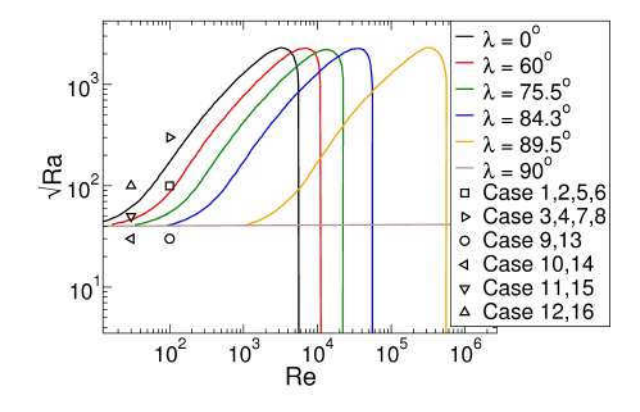


Figure 4. Present unstable and stable square channel flow simulations (symbols) and neutral curves by Gage and Reid. 11

	Dimensions	Re	\sqrt{Ra}	Code	L or Z
Case 1	2-D	100	100	Old	L=2
Case 2	2-D	100	100	New	L=2
Case 3	2-D	100	300	Old	L=2
Case 4	2-D	100	300	New	L=2
Case 5	3-D	100	100	Old	Z=2
Case 6	3-D	100	100	New	Z=2
Case 7	3-D	100	300	Old	Z=2
Case 8	3-D	100	300	New	Z=2
Case 9	2-D	100	30	New	L=12
Case 10	2-D	30	30	New	L=12
Case 11	2-D	30	50	New	L=12
Case 12	2-D	30	100	New	L=12
Case 13	3-D	100	30	New	Z=12
Case 14	3-D	30	30	New	Z=12
Case 15	3-D	30	50	New	Z=12
Case 16	3-D	30	100	New	Z=12

Table 3. Parameters for 2-D and 3-D square channel flow simulations.

provided by the code (new code) or computed using Fourier transforms (old code). Modes are denoted by their streamwise, l, and spanwise, k, mode numbers which are related to the streamwise and spanwise wavelengths via $\lambda_x = L/l$ and $\lambda_z = Z/k$. The streamwise and spanwise domain extents, L and Z, are equivalent to the streamwise and spanwise fundamental wavelengths. Gage and Reid¹¹ do not report the wavenumber of the most unstable 3-D modes. Ostrach and Kamotani²⁹ state that the spanwise wavelength of the most unstable longitudinal waves is roughly two times the channel height.

The disturbance amplitudes for the 2-D validation cases are provided in Fig. 6a. The streamwise mode l=1 grows exponentially (linear growth) until saturation for cases 3 & 4. Identical growth rates are obtained with the old and new code. For the stable cases (1 & 2) the disturbance amplitudes decay. The k=1 mode amplitudes for the 3-D validation cases (5-8) are plotted in Fig. 6b. Since both $\sqrt{Ra} = 100$ and $\sqrt{Ra} = 300$ are above $\sqrt{Ra_c} = \sqrt{1,708} = 41.3$, temporal growth must be expected for both cases. This is in fact the case. As for the 2-D validation cases, good agreement of the growth rates for the results obtained with the old and new code is observed. The growth rates for $\sqrt{Ra} = 300$ are larger than for $\sqrt{Ra} = 100$ which indicates a

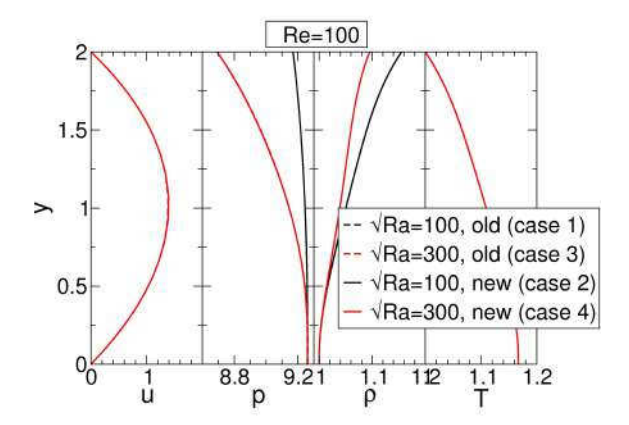


Figure 5. Velocity, pressure, density, and temperature profiles for cases 1-4.

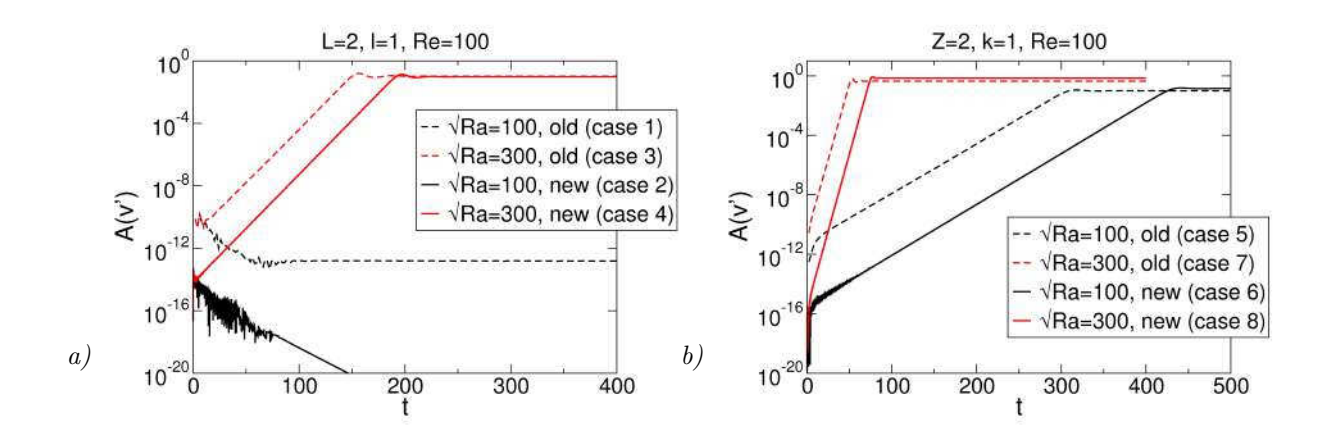


Figure 6. Time evolution of Fourier modes of wall normal disturbance velocity at mid-channel height for a) 2-D cases (case 1-4) and b) 3-D cases (case 5-8).

stronger instability. The results in Fig. 6 also illustrate the high accuracy of the new compact finite difference code. The round-off error is much lower than for the old code and, as a result, the disturbance amplitudes grow from much lower levels.

Eight additional square channel flow simulations (four 2-D cases, 9, 10, 11 & 12, and four 3-D cases, 13, 14, 15 & 16) were performed with the new code (Tab. 3). The fundamental wavelengths in the streamwise and spanwise direction was L=Z=12. Fourier modes of the wall-normal velocity for the 2-D cases are plotted in Fig. 7. For the same Reynolds number (Re=30), case 12 ($\sqrt{Ra}=100$) is unstable while cases 10 ($\sqrt{Ra}=30$) & 11 ($\sqrt{Ra}=50$) are stable. Case 9 (Re=100 and $\sqrt{Ra}=30$) is also stable. For case 12, mode l=3 is most unstable and experiences the largest growth rate. Modes l=4, 2, and 5 are also growing. Possibly as the result of nonlinear interactions, mode 6 (and later other modes) starts to grow as soon as the mode 3 amplitude reaches approximately 3×10^{-8} . For the stable cases (9, 10 and 11) all mode amplitudes decay exponentially in time.

The reference Reynolds number for the 3-D simulations was Re=30 for cases 14, 15 & 16 and Re=100 for case 13. The square root of the Rayleigh number was \sqrt{Ra} =50 and 100 for cases 15 & 16, respectively, which is above the critical Rayleigh number (\sqrt{Ra}_c =41.3) and \sqrt{Ra} =30 for cases 13 & 14. Since the neutral curve for λ =90deg is crossed as the Rayleigh number is increased, disturbance growth must be expected for cases 15 & 16. The present results indicate linear growth for cases 15 and 16 (Fig. 8) and exponential decay for cases 13 and 14 (Fig. 9).

For case 15 (unstable 3-D case) mode k=3 which has a spanwise wavelength of 4 (identical to one-third

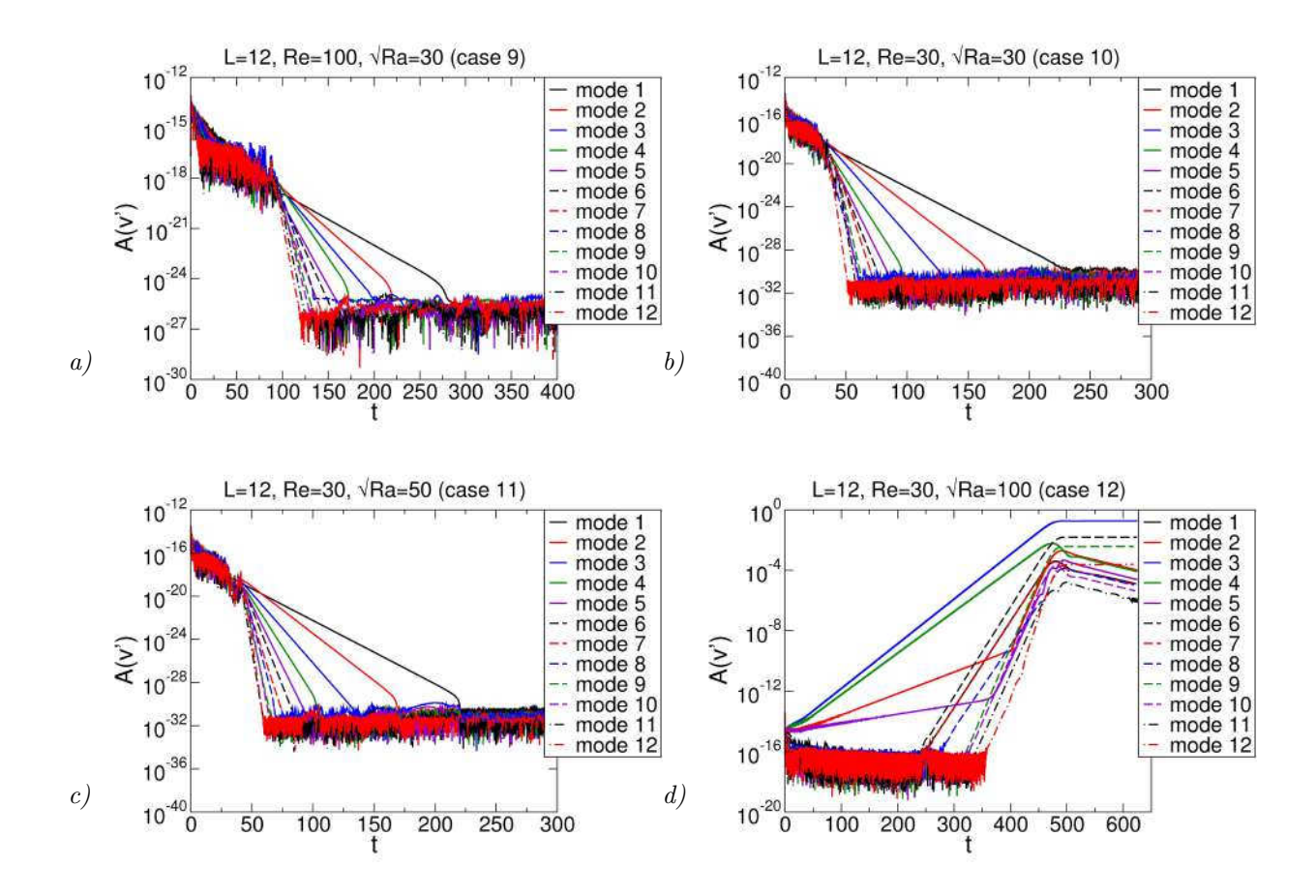


Figure 7. Fourier modes of wall-normal disturbance velocity at mid-channel height for case a) 9, b) 10, c) 11, and d) 12.

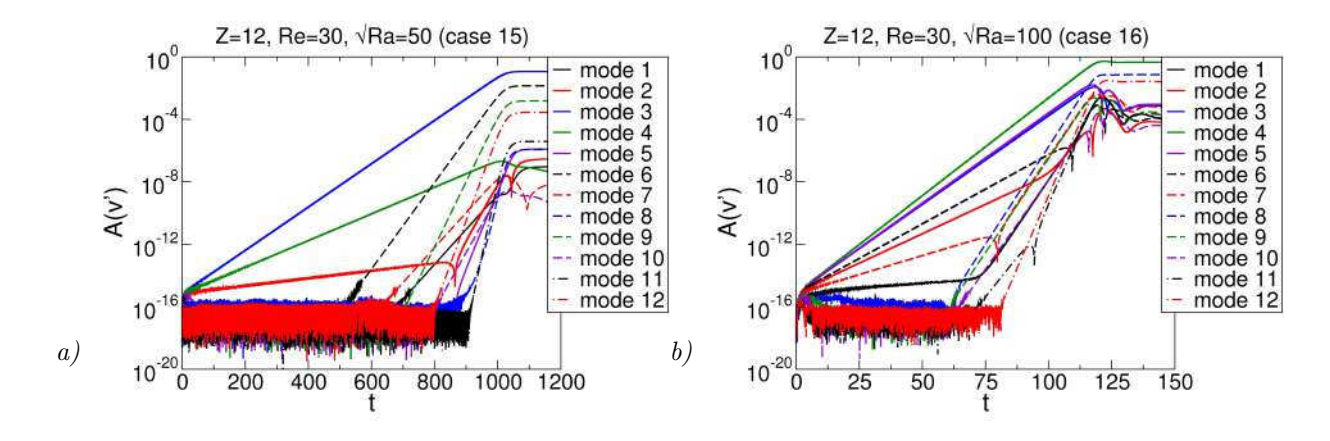


Figure 8. Fourier modes of wall-normal disturbance velocity at mid-channel height for case a) 15 and b) 16.

of the domain width) is experiencing the strongest amplification (Fig. 8a). This result is in agreement with Ostrach and Kamotani²⁹ who reported a wavelength of two times the channel height. Modes 4 and 2 are also unstable. As mode 3 reaches an amplitude of approximately 10^{-8} , mode 6 begins to grow probably as a result of nonlinear interactions. For traveling waves the phase speeds have to match up (phase synchronization) for resonance to occur. Modes 3 & 6 are both steady waves and this criterion is therefore satisfied. As the mode

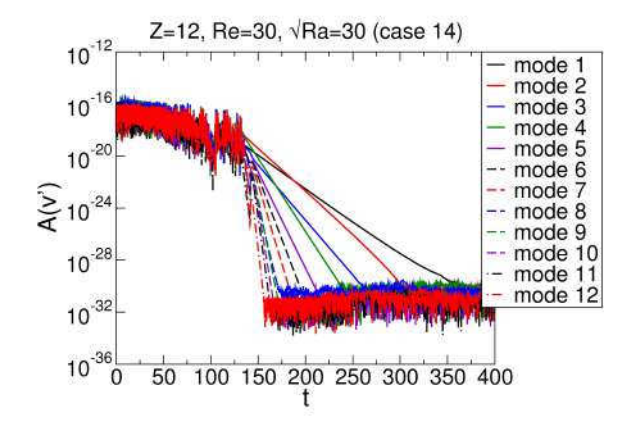


Figure 9. Fourier modes of wall-normal disturbance velocity at mid-channel height for case 14.

amplitudes saturate, six longitudinal convection rolls appear that are aligned in the streamwise direction (Fig. 10a). Shown are iso-surfaces of the Q-criterion flooded by the velocity magnitude. The Q-criterion,³⁰

$$Q = \frac{1}{2} \left(W_{i,j} W_{i,j} - S_{i,j} S_{i,j} \right) , \tag{59}$$

is used to identify vortical flow structures. Here,

$$S_{i,j} = \frac{1}{2} \left(u_{i,j} + u_{j,i} \right) \,, \tag{60}$$

is the strain rate tensor and

$$W_{i,j} = \frac{1}{2} \left(u_{i,j} - u_{j,i} \right) \,, \tag{61}$$

is the rotation rate tensor. The temperature iso-contours in Fig. 10b illustrate how the longitudinal rolls transport hot air from the bottom surface (350K) to the top surface (300K). Interestingly, for the other unstable case (case 16) mode 4 is slightly more amplified than mode 3 (Fig. 8b). Contrary to Ostrach and Kamotani²⁹ the wavelength of the most unstable mode (k=4) is found to be 3 (1.5 times the channel height).

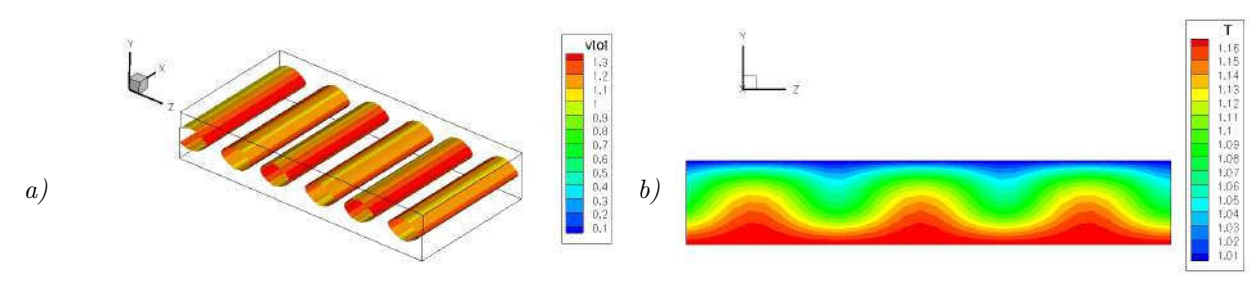


Figure 10. Case 15: a) Iso-surfaces of Q=0.01 flooded by velocity magnitude and b) temperature iso-contours in x=const. plane.

B. Simulation of Entire SCPP and Collector Simulations

The collector and the chimney are the two main components of SCPPs. An earlier implicit large eddy simulation (ILES) by Meng et al.²² of the SCPP experiment at the University of Arizona⁵ was continued. The reference Mach number for the simulation is very small (M=0.001) which limits the computational time step since the Courant-Friedrichs-Lewy (CFL) number scales with the inverse of the Mach number (for M=0.001, the acoustic waves are 1,000 faster than the reference velocity). This makes the simulation computationally expensive. It was estimated that 80,000 time steps are required for one "flow-through time" (i.e., time that it takes for one fluid particle to travel from the collector inlet to the chimney outlet).

Since the focus of the present investigations is on the collector, it was decided to carry out new simulations for the collector only. By disregarding the chimney in the simulations, the computational expense is reduced. In addition, the reference Mach number was raised to M=0.05 to allow for a larger time step which shortens the simulation turnaround times.

The circumferential area in the collector scales with $2\pi rh$ where h is the collector height and r is the radius measured from the center of the collector. Thus, for incompressible flow (ρ =const.) the velocity inside the collector varies according to $v \propto 1/r$ (radial continuity equation) and as a result the Reynolds number increases hyperbolically as the chimney inlet is approached. The collector exit Mach number for the present collector simulation (reference Mach number M=0.05) is approximately 0.21. Since M=0.3 is commonly considered the limit for incompressible flow, this outflow Mach number was considered acceptable.

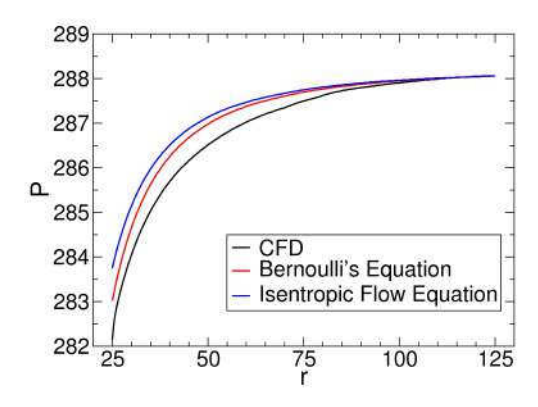


Figure 11. Pressure inside collector for collector simulation.

In Fig. 11 the static pressure inside the collector is plotted versus the radial coordinate (r=0 is at the center of the collector). The pressure extracted from the simulation ("CFD") is compared with the pressure computed from the velocity, v_2 , and temperature, T_2 , inside the collector. For low Mach number flows Bernoulli's equation may be invoked,

$$p_1 + \frac{1}{2}\rho v_1^2 = p_2 + \frac{1}{2}\rho v_2^2. (62)$$

Here, v_1 and p_1 are the conditions at the collector inflow. The present CFD result ("CFD") and the pressure, $p_2(v_2)$, computed from Bernoulli's equation ("Bernoulli's Equation") are in reasonable agreement (Fig. 11).

Assuming a constant total enthalpy (strictly speaking, this is not the case since the walls are not adiabatic and the flow is not inviscid), the temperature, T_2 , can be computed from the velocity, v_2 , via

$$c_p T_1 + \frac{v_1^2}{2} = c_p T_2 + \frac{v_2^2}{2} \,,$$
(63)

where $c_p = 1/[(\gamma - 1)M^2]$ is the specific heat at constant pressure, and M and γ are the reference Mach number and ratio of specific heats, respectively. Assuming isentropic flow (which is an approximation that neglects both physical and numerical diffusion), the pressure, p_2 , ("Isentropic Flow Equation" in Fig. 11) can then be obtained from,

$$\frac{p_1}{p_2} = \left(\frac{T_1}{T_2}\right)^{\frac{\gamma}{\gamma - 1}}.\tag{64}$$

The agreement with the static pressure from the simulation ("CFD") is again reasonable (Fig. 11).

The pressure drop towards the collector outlet is very small ($\approx 2\%$ of the inflow static pressure, Fig. 11). The pressure drop in the collector is balanced by the pressure difference created by the chimney effect and the pressure difference across the turbines. The pressure difference (inlet to outlet) for a chimney of height H can be obtained from the chimney formula,

$$\Delta p = q(\rho_a - \rho_i)H, \tag{65}$$

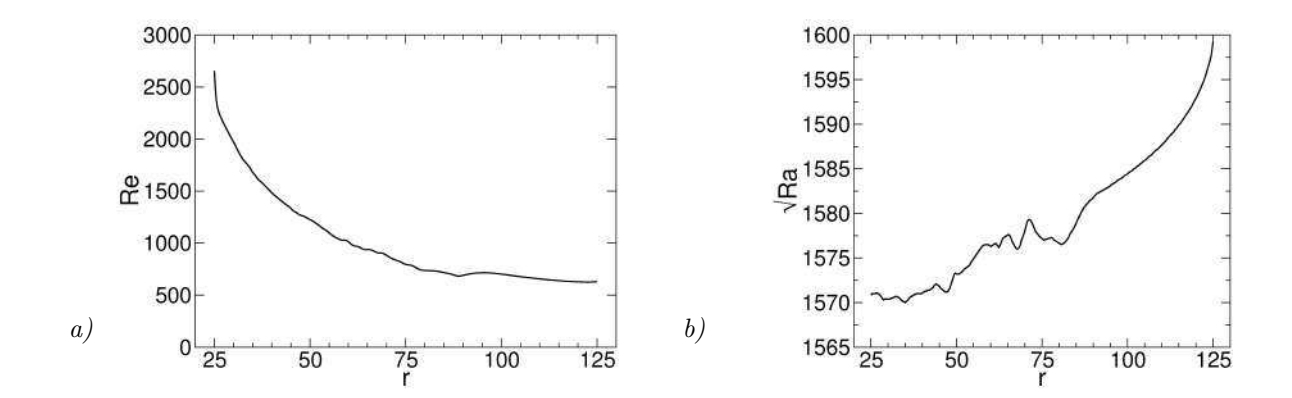


Figure 12. a) Reynolds number and b) square root of Rayleigh number for collector simulations.

where ρ_a and ρ_i are the ambient and chimney inlet density, respectively. This pressure difference is driving the collector flow.

In Fig. 12 the local Reynolds number, Re, and square root of the Rayleigh number, \sqrt{Ra} , based on the maximum local radial velocity and the collector half height (same reference velocity and length scale as in Gage and Reid¹¹) are plotted versus the radial coordinate. Because the radial velocity increases in the streamwise direction, the Reynolds number increases from about 700 (collector inflow, r=125) to about 2,700 at the collector outflow (r=25).

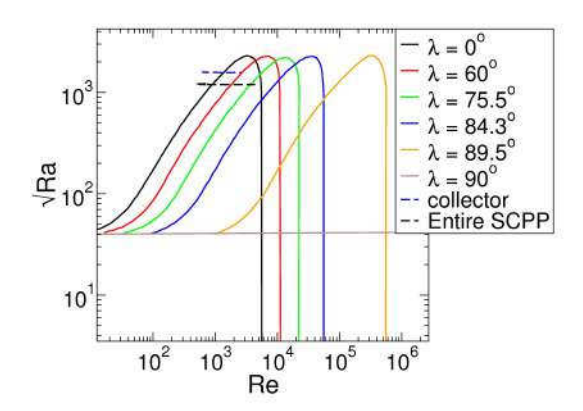


Figure 13. Reynolds and Rayleigh number distributions for present simulations overlaid on neutral curves by Gage and ${\rm Reid.}^{11}$

In Fig. 13 the Reynolds number, Re, and square root of the Rayleigh number, \sqrt{Ra} , for the present simulations (simulation of entire SCPP and collector simulations) are compared with the neutral curves by Gage and Reid.¹¹ The Reynolds number for the simulations is slightly below the critical Reynolds number for the viscous instability ($Re < Re_c = 5,400$). The Rayleigh number, on the other hand, is far above the critical Rayleigh number for buoyancy driven instability ($Ra > Ra_c = 1,708$). Since the $\lambda = 0$ deg waves are the most unstable waves, longitudinal rolls must be expected.

Two collector simulations were carried out. For the first simulation, disturbances were growing from machine round-off ("natural" undisturbed flow). In the experiment the collector roof is supported by screws which introduce steady streamwise disturbances at the collector inlet. Wind loads acting on the collector roof may result in minute structural vibrations which might introduce unsteady disturbances at the inflow. Therefore, for the second simulation, a steady and an unsteady disturbance,

$$v' = v'_{steady} + v'_{unsteady}, (66)$$

were introduced ("forced" case) via wall-normal blowing and suction with velocity, v', on the collector bottom wall for $r_1 = 123.9 > r > r_2 = 116.0$. The steady disturbances had an amplitude of A=0.1 and an azimuthal mode number of eight,

$$v'_{steady} = Af(r)\sin\left(2\pi \frac{8\varphi}{15deg}\right), \tag{67}$$

where φ is the azimuthal coordinate. The amplitude for the unsteady disturbances was A=0.1,

$$v'_{unsteady} = Af(r)\sin(2\pi t), \qquad (68)$$

where t is time. The disturbance amplitude was varied in the streamwise direction according to,

$$f(r) = \begin{cases} 5.0625(1+x)^3 \left[3(1+x)^2 - 7(1+x) + 4 \right] & x < 0 \\ -5.0625(1-x)^3 \left[3(1-x)^2 - 7(1-x) + 4 \right] & x > 0 \end{cases}$$
 (69)

with $x = -1 + 2(r - r_1)/(r_2 - r_1)$.

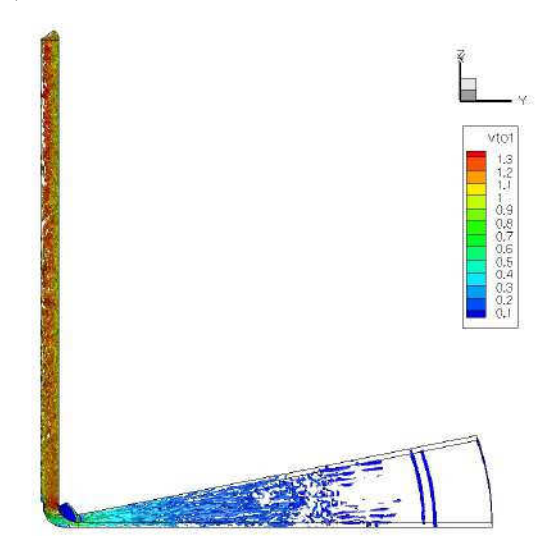


Figure 14. Instantaneous iso-surfaces of Q=0.1 flooded by velocity magnitude (simulation of entire SCPP).

An instantaneous flow visualization for the simulation of the entire SCPP is provided in Fig. 14. The flow visualization reveals transverse rolls near the collector inlet and longitudinal rolls about half way into the collector. Instantaneous flow visualizations for the collector simulations are provided in Fig. 15. Eight

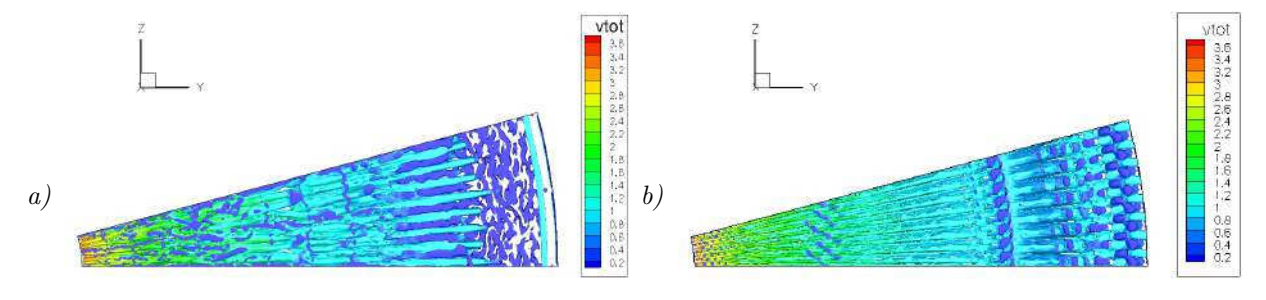


Figure 15. Instantaneous Q iso-surfaces flooded by velocity magnitude (collector simulations). a) "natural" undisturbed flow (Q=0.00001) and b) disturbed flow (Q=0.02).

longitudinal rolls (per 15deg segment) appear downstream of the inflow for both collector simulations ("natural" and "forced" case). The unsteady disturbances for the "forced" case appear to get damped in the streamwise direction which was expected because $Re < Re_c = 5,400$. However, about two thirds into the collector unsteady flow structures reappear. It may be speculated that the primary 3-D disturbances have saturated and that a secondary instability occurs. This will be investigated in the future.

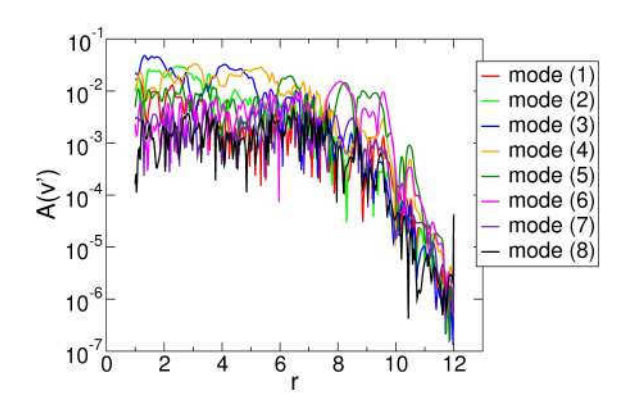


Figure 16. Instantaneous azimuthal Fourier modes of wall normal velocity for simulation of entire SCPP.

Since the Rayleigh number is above $Ra_c = 1,708$, azimuthal 3-D disturbances (wave angle, λ =90deg) must be expected. Therefore, azimuthal Fourier transforms of the instantaneous wall-normal velocity at the mid collector height were performed to analyze the streamwise growth of the 3-D waves. Different from the square-channel flow simulations (temporal stability analysis), the instability waves in the collector simulation are growing in the downstream direction (spatial stability analysis). Azimuthal Fourier modes for the simulation of the entire SCPP are shown in Fig. 16. Initially (near the inflow) modes k=5 & 6 have the largest amplitudes. Further into the collector modes 3 & 4 are dominant and finally near the collector outflow mode 2 attains an appreciable amplitude. Based solely on the flow visualization in Fig. 14 this behavior may be interpreted as "vortex merging".

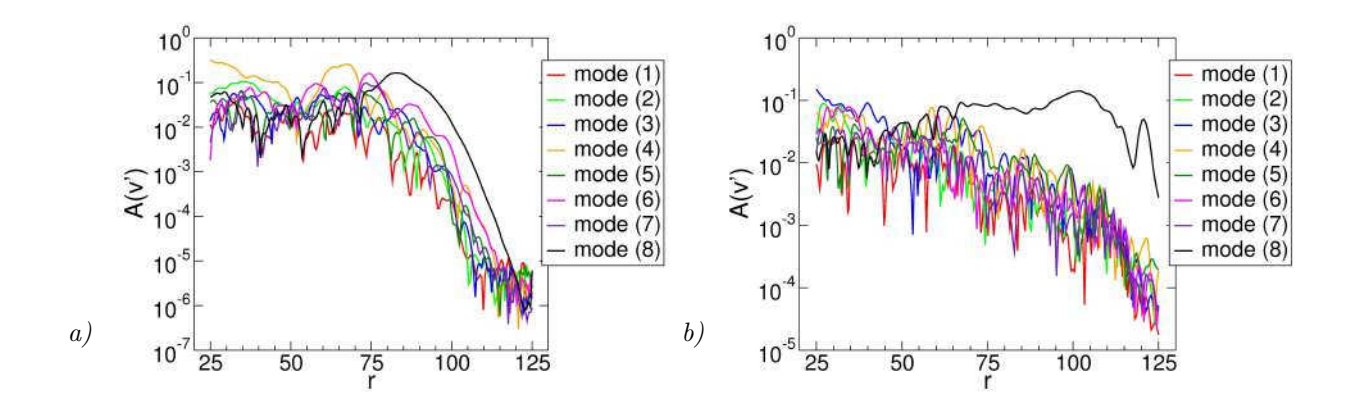


Figure 17. Instantaneous azimuthal Fourier modes of wall-normal velocity for collector simulation a) "natural" case and b) "forced" case.

For the undisturbed ("natural") collector simulation, spanwise mode k=8 is amplified first and grows approximately exponentially ("linear" growth) up to $r \approx 80$ (Fig. 17a). Modes 1-7 are also growing but their amplitudes are about one order of magnitude lower than for mode 8. The amplitudes of modes 4 & 6 are slightly larger than the amplitudes of modes 1-3, 5, and 7. It may be argued that modes 4 & 6 are unstable. Alternatively, it may be argued that the mode 8 amplitude is already large enough to result in nonlinear interactions. For r < 80 mode 8 decays and mode 6 and later mode 4 become dominant (largest mode amplitudes). Based on the flow visualization (Fig. 15a) this behavior may be interpreted as "vortex merging". Near $r \approx 35$ the amplitude of mode 2 is almost as large as the amplitude of mode 4.

Because mode 8 experiences the strongest amplification for the "natural" case, it was introduced at the collector inflow for the "forced" case. For the "forced" case an adjustment of the mode 8 amplitude over

the forcing slot is observed for 116 < r < 124. Downstream of the disturbance slot mode 8 is growing exponentially. Because of the higher initial amplitude mode 8 is saturating earlier $(r \approx 105)$ than for the "natural" case. For $r\approx55$ mode 4 is dominant and for $r\approx40$ mode 3 is dominant. Overall, for r>70 the disturbance amplitudes are much higher than for the "natural" case.

IV. Conclusions

The radial Rayleigh-Bénard-Poiseuille (RBP) flow inside the collector of solar chimney power plants (SCPPs) may be subject to buoyancy driven and viscous instabilities. Modal growth may lead to longitudinal or transverse rolls that could greatly enhance the wall-normal momentum and heat transfer and thus have a profound effect on the collector performance. Information about the stability of the collector flow may be gained from linear stability theory (LST) analyses (e.g., Gage and Reid¹¹) or from local stability simulations such as proposed here. For the stability simulations, first a base flow profile is computed and then disturbances with very small "linear" amplitudes are introduced. Square channel flow stability simulations were carried out with an existing versatile but "noisier" finite-volume code and with a newly developed problem-specific "clean" compact finite difference code. The results from the stability simulations agree well with each other and with the Gage and Reid¹¹ LST results.

The finite-volume code was also employed for investigating the radial flow inside the collector of a 1:30 scale model of the Manzanares SCPP which has been erected on the roof of the Aerospace and Mechanical Engineering Department at the University of Arizona.⁵ Simulations were carried out for the full SCPP (collector and chimney) and for the collector only. It was determined that the Reynolds number, Re, inside the collector remains below the critical Reynolds number for viscous instability to occur ($Re_c = 5,400$). The Rayleigh number, however, is far larger than the critical Rayleigh number for buoyancy driven instability ($Ra_c = 1,708$) and longitudinal rolls appear. The present collector simulations indicate that the flow inside the collector is subject to a buoyancy-driven convective instability. Therefore, the inflow disturbance amplitudes have a strong influence on the onset and character of the nonlinear interactions. Based on a Fourier analysis of the disturbances and instantaneous flow visualizations it is suggested that "vortex merging" may occur in the streamwise direction. A similar finding was made earlier by Meng et al.²² Despite the fact that the Reynolds number remains below the critical Reynolds number, unsteady flow structures appear as the outflow is approached which may indicate the presence of a secondary instability.

Much remains to be done. The new compact finite difference code will be developed further to allow for stability investigations of radial RBP flows. Stability investigations will be carried out for the conditions of the 1:30 scale experiment at the University of Arizona⁵ to allow for a direct comparison with the experiment and with the finite-volume code simulations. The data obtained from the collector simulations will be Fourier transformed in time and analyzed w.r.t. the unsteady flow structures. The measurements at the University of Arizona will provide information about the inflow disturbances which were found to have a deciding impact on the flow structures inside the collector.

Acknowledgments

This material is based upon work supported by the National Science Foundation under grant no. 1510179. The program manager is Dr. Ronald Joslin. This work used the Extreme Science and Engineering Discovery Environment (XSEDE) which is supported by the National Science Foundation under grant no. ACI-1053575.

References

¹Schlaich, J., "The Solar Chimney Electricity from the Sun," Eds. F.W. Schubert and J. Schlaich, Edition Axel Menges, 1995, Deutsche Verlagsanstalt, Stuttgart, 1994, C. Maurer, Geislingen, Germany

²Haaf, W., Friedrich, K., Mayr, G., and Schlaich, J., "Solar chimneys, part I: principle and construction of the pilot plant in Manzanares," *International Journal of Sustainable Energy*, Vol. 2, No. 1, 1983, pp. 3-22

³Haaf, W., "Solar chimneys, part II: preliminary test results from the Manzanares pilot plant," *International Journal of Solar Energy*, Vol. 2, 1984, pp. 141-161

⁴Schlaich, J., Bergermann, R., Schiel, W., and Weinerbe, G., "Design of commercial solar updraft tower systems-utilization of solar induced convective flows for power generation," *Journal of Solar Energy Engineering*, Vol. 127, 2005, pp. 117-124

⁵Fasel, H.F., Meng, F., and Gross, A., "Numerical and Experimental Investigation of 1:33 Scale Solar Chimney Power Plant," 11th International Conference on Heat Transfer, Fluid Mechanics, and Thermodynamics, South Africa, 20-23 July 2015. URI: http://hdl.handle.net/2263/55874

- ⁶Pastohr, H., Kornadt, O., and Gurlebeck, K., "Numerical and analytical calculations of the temperature and flow field in the upwind power plant," *International Journal of Energy Research*, Vol. 28, 2004, pp. 495-510
- ⁷Ming, T., Liu, W., and Xu, G., "Analytical and numerical investigation of the solar chimney power plant systems," *International Journal of Energy Research*, Vol. 30, 2006, pp. 861-873
- ⁸Ming, T.Z., Liu, W., Pan, Y., and Xu, G.L., "Numerical analysis of flow and heat transfer characteristics in solar chimney power plant with energy storage layers," *Energy Conversion and Management*, Vol. 49, 2008, pp. 2872-2879
- ⁹Ming, T., Wang, X., de Richter, R.K., Liu, W., Wu, T., and Pan, Y., "Numerical analysis on the influence of ambient crosswind on the performance of solar updraft power plant system," *Renewable and Sustainable Energy Reviews*, Vol. 16, 2012, pp. 5567-5583
- ¹⁰Xu, G., Ming, T., Pan, Y., Meng, F., and Zhou, C., "Numerical analysis on the performance of solar chimney power plant system," *Energy Conversion and Management*, Vol. 52, 2011, pp. 876-883
- ¹¹Gage, K.S., and Reid, W.H., "The stability of thermally stratified plane Poiseuille flow," *Journal of Fluid Mechanics*, Vol. 33, part I, 1968, pp. 21-32
- ¹²Akiyama, M., Hwang, G.J., and Cheng, K.C., "Experiments on the onset of longitudinal vortices in laminar forced convection between horizontal blades," *Journal of Heat Transfer*, Vol. 93, 1971, pp. 335-341
- ¹³Nicolas, X., Zoueidi, N., and Xin, S., "Influence of a white noise at channel inlet on the parallel and wavy convective instabilities of Poiseuille-Rayleigh-Bénard flows," *Physics of Fluids*, Vol. 24, 2012, pp. 084101
- ¹⁴Fujimura, K., and Kelly, R.E., "Interaction between longitudinal convection rolls and transverse waves in unstably stratified plane Poiseuille flow," *Physics of Fluids*, Vol. 7, No. 1, 1995, pp. 68-79
- ¹⁵Luijkx, J.-M., Platten. J.K. and Legros, J.C., "On the existence of thermoconvective rolls, transverse to a superimposed mean Poiseuille flow," *International Journal of Heat and Mass Transfer*, Vol. 24, 1981, pp. 1287-1291
- ¹⁶Nicolas, X., Luijkx, J.-M., and Platten. J.-K., "Linear stability of mixed convection flows in horizontal rectangular channels of finite transversal extension heated from below," *International Journal of Heat and Mass Transfer*, Vol. 43, 2000, pp. 589-610
- $^{17}\mathrm{L\"{u}cke},$ M., and Kamps, M., "Transversal convection patterns in horizontal shear flow," Physical Review A, Vol. 45, 1992, pp. 3714-3726
- ¹⁸Carriére, P., and Monkewitz, P.A., "Convective versus absolute instability in mixed Rayleigh-Bénard-Poiseuille convection," *Journal of Fluid Mechanics*, Vol. 384, 1999, pp. 243-262
- ¹⁹Van Santen, H., Kleijn, C.R., and Van Den Akker, H.E.A., "Mixed convection in radial flow between horizontal plates-I. Numerical simulations," *International Journal of Heat and Mass Transfer*, Vol. 43, 2000, pp. 1523-1535
- ²⁰Van Santen, H., Kleijn, C.R., and Van Den Akker, H.E.A., "Mixed convection in radial flow between horizontal plates-II. Experiments," *International Journal of Heat and Mass Transfer*, Vol. 43, 2000, pp. 1537-1546
- ²¹Fasel, H., Meng, F., Shams, E., and Gross, A., "CFD analysis for solar chimney power plants," Solar Energy, Vol. 98, 2013, pp. 12-22
- ²²Meng, F., Gross, A., and Fasel, H.F., "Computational Fluid Dynamics Investigation of Solar Chimney Power Plant," AIAA-Paper AIAA 2013-2460, 2013
- ²³Towns, J., Cockerill, T., Dahan, M., Foster, I., Gaither, K., Grimshaw, A., Hazlewood, V., Lathrop, S., Lifka, D., Peterson, G.D., Roskies, R., Scott, J.R., and Wilkins-Diehr, N., "XSEDE: Accelerating Scientific Discovery," *Computing in Science and Engineering*, Vol. 16, No. 5, 2014, pp. 62-74, doi:10.1109/MCSE.2014.80.
- $^{24} {\rm Gross},$ A., and Fasel, H.F., "High-Order Accurate Numerical Method for Complex Flows," AIAA Journal, Vol. 46, No. 1, 2008, pp. 204-214
- ²⁵Sorensen, H., Jones, D., Heideman, M., and Burrus, C., "Real-valued fast Fourier transform algorithms," *IEEE Transactions ASSP*, Vol. 35, No. 6, June 1987, pp. 849-864
 - ²⁶Mitra, S.J., and Kaiser, J.F., "Digital Signal Processing Handbook," Chap. 8, 1993, John Wiley & Sons, pp. 491-610
 - ²⁷Fyfe, D.J., "Economical Evaluation of Runge-Kutta Formulae," Mathematics of Computation, Vol. 20, 1966, pp. 392-398
 - ²⁸Gross, A., and Fasel, H.F., "Characteristic Ghost Cell Boundary Condition," AIAA Journal, Vol. 45, 2007, pp. 302-306
- ²⁹Ostrach, S., and Kamotani, Y., "Heat Transfer Augmentation in Laminar Fully Developed Channel Flow by Means of Heating From Below," *Journal of Heat Transfer*, Vol. 97, No. 2, 1975, pp. 220-225
- ³⁰Hunt, J.C.R., Wray, A.A., and Moin, P., "Eddies, stream and convergence zones in turbulent flows," Report CTR-S88, Center for Turbulence Research, Stanford, CA, 1988